ARTICLE NO. 78-1310R

Annular Suspension and Pointing System

Willard W. Anderson,* Nelson J. Groom,† and Charles T. Woolley†
NASA Langley Research Center, Hampton, Va.

The Annular Suspension and Pointing System (ASPS) is a general-purpose mount designed to provide orientation, mechanical isolation, and fine pointing for space experiments. The ASPS consists of two assemblies, the first being a set of two gimbals attached to a carrier spacecraft (e.g., Space Shuttle) and providing coarse pointing, and the second a magnetic vernier-pointing and isolation assembly attached to the inner gimbal of the first assembly and providing fine pointing. Discussion of the evolution of this concept, required technology, and data from analyses and simulations predicting pointing accuracies that allowed the specification of hardware design requirements is presented.

Nomenclature

D_{EC} = transformation from shuttle to elevation gimbal coordinates
D_{LE} = transformation from elevation to lateral gimbal coordinates
F_A = total axial centering force acting on the payload
F_{A1} = centering force produced by axial bearing 1
F_{A2} = centering force produced by axial bearing 2
F_B = force produced by bottom electromagnet
F_C = command force
$\bar{F}_{MBA}$ = forces produced by magnetic bearings
F_R = radial payload centering force
F_T = force produced by top electromagnet
G = bearing-gap displacement
$\bar{H}_C, \bar{H}_E, \bar{H}_L, \bar{H}_{PL}$ = angular momentum of shuttle, elevation gimbal, lateral gimbal, and payload
I_C, I_E, I_L, I_{PL} = inertia of shuttle, elevation gimbal, lateral gimbal, and payload
I_C^E = inertia of elevation gimbal transformed to shuttle system
I_C^L = inertia of lateral gimbal transformed to shuttle system
I_C^{CEL} = sum of inertias of shuttle, elevation gimbal, and lateral gimbal in shuttle coordinates
K = electromagnet constant, Eq. (1)
K_B = equivalent electromagnet gain, Eq. (3)
$KE_C, KE_E, KE_L, KE_{PL}$ = kinetic energy of shuttle, elevation gimbal, lateral gimbal, and payload
KE_{CEL} = total kinetic energy of shuttle and coarse gimbals
K_M = equivalent unbalanced bias-flux stiffness, Eq. (3)
L = distance of payload center of mass from payload plate
M = suspended mass
M_C, M_E, M_L, M_{PL} = mass of shuttle, elevation gimbal, lateral gimbal, and payload
M_{EL} = sum of elevation and lateral gimbal masses
M_{CEL} = total mass of shuttle and coarse gimbals
M_P = control moment produced by axial actuators
$\bar{P}_C, \bar{P}_{PL}$ = linear momentum of shuttle and payload
R = radius of ASPS rim
$\bar{R}_C^E$ = vector which defines the origin of the elevation-lateral system in shuttle coordinates
$\bar{R}_{PL}^B$ = vector which defines the base of the payload in the payload coordinates
s = Laplace variable
$\bar{T}_C, \bar{T}_E, \bar{T}_L$ = torques applied to shuttle, elevation gimbal, and lateral gimbal
$\bar{T}_{MBA}$ = torques produced by magnetic bearings
$\bar{V}_C, \bar{V}_E, \bar{V}_L, \bar{V}_{PL}$ = velocities of shuttle, elevation gimbal, lateral gimbal, and payload centers of mass expressed in their respective coordinates
$\theta_E, \dot{\theta}_E$ = elevation gimbal angle and time rate of change of same
θ_G = coarse gimbal angle
$\phi_L, \dot{\phi}_L$ = lateral gimbal angle and time rate of change of same
$\bar{\omega}_C, \bar{\omega}_E, \bar{\omega}_L, \bar{\omega}_{PL}$ = body rates of shuttle, elevation gimbal, lateral gimbal, and payload

Presented as Paper 78-1310 at the AIAA Guidance and Control Conference, Palo Alto, Calif., Aug. 7-9, 1978; submitted Aug. 28, 1978; revision received Feb. 5, 1979. Reprints of this article may be ordered from AIAA Special Publications, 1290 Avenue of the Americas, New York, N.Y. 10019. Order by Article No. at top of page. Member price $2.00 each, nonmember, $3.00 each. **Remittance must accompany order.**

Index categories: Spacecraft Systems; Spacecraft Dynamics and Control.

*Assistant Chief, Flight Dynamics and Control Division.
†Aero-Space Technologist, Stability and Control Branch, FDCD.

Introduction

THE need for a multipurpose experiment pointing platform was established during NASA Earth-orbital systems technology guidance and control planning activities during the early 1970's. The Annular Suspension and Pointing System (ASPS) concept was developed to meet this need. The ASPS is a derivative of the Annular Momentum Control Device (AMCD) which is described in Ref. 1. A detailed description along with linear analyses of the ASPS system are presented in Ref. 2. Although the AMCD and ASPS share a common magnetic bearing design and suspension technique, the two are very different in purpose and operation. The differences are sufficiently great that the ASPS is considered a unique device on its own.[3] This paper presents a general discussion of the ASPS concept and a discussion of the evolution of the concept that lead to a decision by NASA to build a prototype ASPS for use on the Space Shuttle.

Background Research

The AMCD represents a new concept in momentum storage devices and is proposed for the control and stabilization of spacecraft. The basic AMCD concept, shown schematically in

Fig. 1, consists of a spinning rim with no central hub section suspended by a minimum of three noncontacting magnetic support stations and driven by a noncontacting electromagnetic spin motor. Because of its unique configuration, the AMCD possesses an optimum momentum-to-weight ratio, and thus offers the potential for large weight savings over conventional momentum storage devices. In addition, since the central portion of the AMCD is not utilized to achieve the required momentum, this area can be employed to mount other equipment, such as electronics, thus maximizing space utilization and reducing volumetric requirements (large radial dimensions also become feasible). Since the AMCD makes use of noncontacting elements for suspension, for rotor position sensing, and for driving the rotor, no wear mechanism exists and therefore lifetime characteristics are improved over conventional momentum devices. By gimballing the rim in the magnetic bearings, the AMCD can also provide fine-pointing control about two axes.

In order to demonstrate the feasibility of the AMCD concept, a laboratory test model was built and is being used as part of a continuing AMCD hardware technology development. This model, shown in Fig. 2, consists of a graphite/epoxy composite rim, three magnetic bearing suspension stations, three spin motor stator elements (one per bearing station), and six pneumatic backup bearings (required for lab use only). The bearing assemblies are attached to an aluminum base plate. A vacuum cover fits over the bearing-motor-rim assembly and bolts to the base plate for high-speed spin tests. The rim is 1.7 m (5.5 ft) in diameter, weighs 2.4 N (50 lb), and is designed to rotate at 3000 rpm. The rim momentum at this speed is 4068 N-m-s (3000 ft-lb-s). A detailed description of the laboratory test model AMCD is given in Ref. 4.

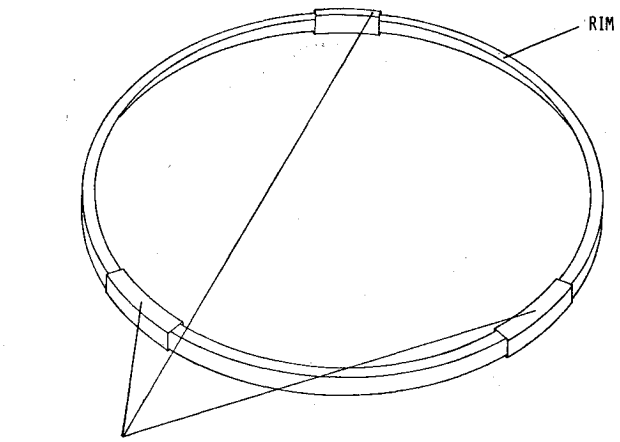

Fig. 1 Annular momentum control device concept.

Early in the development stage of the AMCD, it was recognized that certain characteristics of the concept could be applied to a nonspinning experiment pointing system. In particular, the three areas that made the AMCD configuration applicable to an experiment pointing system were the capability for vernier gimballing of the rim within the magnetic bearing gaps, the natural isolation of the rim through the magnetic bearings, and the existence of roll freedom of the rim. Thus, if the rim was used in a manner such that an experiment package was attached to it and provision for accurate control of the rim about the roll axis was also made, this would constitute a highly accurate pointing system, with vernier gimballing capabilities and roll control.

At first, the ASPS was configured with the rim surrounding the experiment with the experiment center of mass located in the plane of the rim (i.e., c.g. mount) as shown in Fig. 3. However, the multimission requirement for the mount to handle large payloads and payloads of many different shapes, and also a desire not to impose rigid requirements for c.g. control on the experiment developers, made an end-mount configuration appear desirable. A control system feedforward concept was introduced to allow the end-mount magnetic system to have the same performance as the c.g.-mount magnetic system.[2]

Analyses and simulations were performed which showed that the required accuracies were achievable if the magnetic bearings were linear with respect to the actual-force vs input-force transfer function. Methods were then investigated to determine the feasibility of a practical implementation of linear magnetic bearings.

As described in Ref. 4, the AMCD lab model magnetic bearings used permanent magnets to provide flux biasing of the electromagnets. Two of the reasons for selecting permanent magnet flux biasing were: 1) a linear relationship

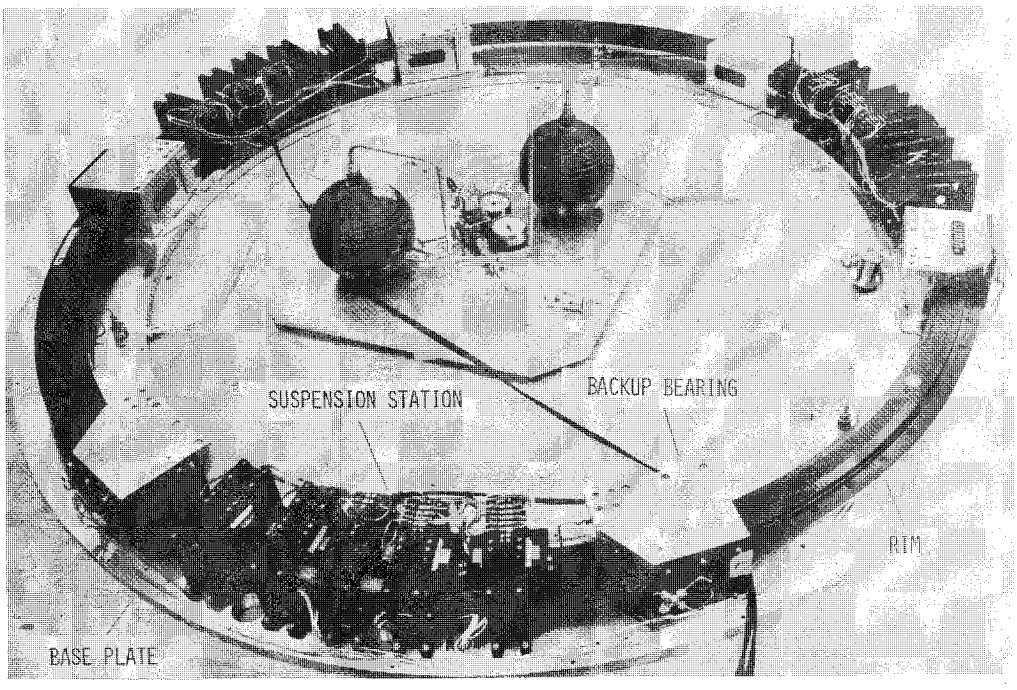

Fig. 2 AMCD laboratory test model.

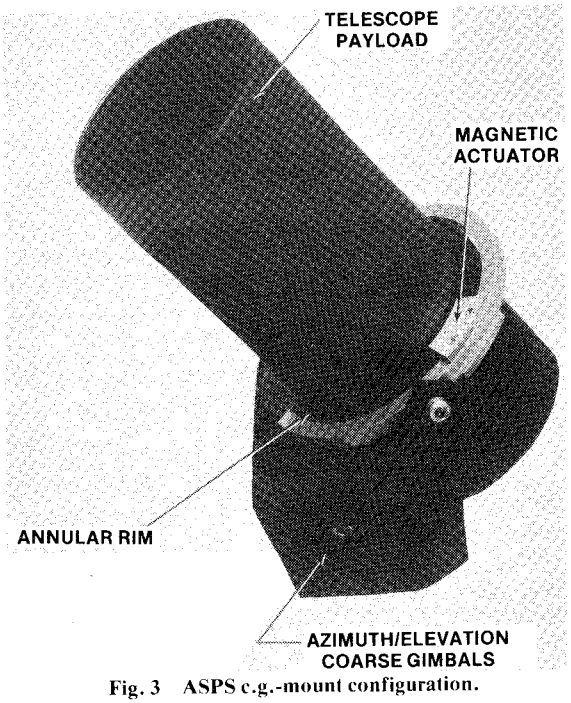

Fig. 3 ASPS c.g.-mount configuration.

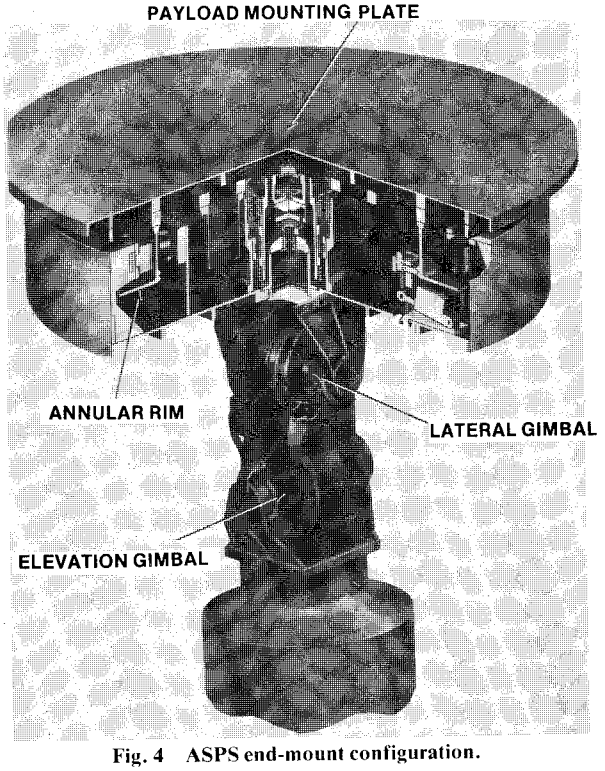

Fig. 4 ASPS end-mount configuration.

between force and current could easily be obtained at a given bearing gap; and 2) with permanent magnets supplying the bias, less power is required to support a given mass in a laboratory 1-g environment. Permanent magnet flux biasing does, however, present several problems from the standpoint of application to the ASPS. First, since the bias flux is fixed, the linear operating range of the bearing is restricted to a small area around a nominal operating point. Second, for a given equivalent permanent magnet stiffness, a minimum bearing-servo-bandwidth is required for stability.[5] For a reasonable actuator force capability, this fixed bandwidth could be high enough to cause servo noise and/or structural interaction problems. These problems led to the consideration

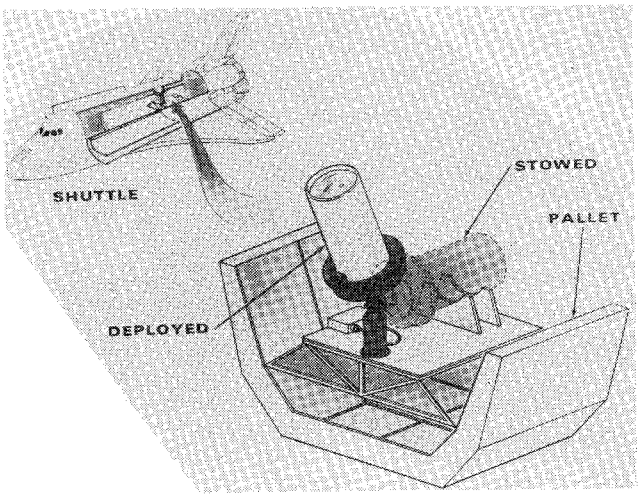

Fig. 5 Shuttle payload configuration for ASPS.

of magnetic flux bias produced by variable currents in the electromagnet coils. This concept was investigated by analysis and a model of the bearing was developed. This model was then used in a simulation of the entire pointing system and the pointing accuracies required were shown to be achievable. Based on these analyses and simulation, a decision was made to develop the annular suspension and pointing system prototype as an end mount.

ASPS End-Mount Concept Description

The ASPS[2] consists of assemblies of coarse and vernier pointing as shown in Fig. 4. The first assembly is attached to a carrier spacecraft (e.g., the Space Shuttle) and consists of two gimbals which provide "coarse" pointing or orientation of the payload instrument by allowing two rotations of the instrument relative to the carrier vehicle (see Fig. 5). Each of these gimbals contains a torque motor and position and rate feedback sensors to allow closed-loop control about the gimbal's axis. The second or vernier pointing assembly is made up of magnetic actuators for suspension and fine pointing, roll-motor segments, and an instrument or experiment mounting plate, around which is attached a continuous annular rim. The rim provides appropriate magnetic circuits for the actuators and the roll-motor segments and allows any roll position of the payload instrument to be selected. The vernier pointing assembly is attached to the second coarse gimbal and provides vernier attitude fine pointing and roll positioning of the experiment as well as six-degree-of-freedom (6-DOF) isolation from carrier motion disturbances. In addition, the vernier pointing assembly has a rim centering mode in which axial and radial rim position sensors located at each actuator station are used to center the rim axially and radially between actuator pole faces. This mode allows coarse gimbal slewing for retargeting, for Earth pointing, or for backup coarse gimbal pointing.

Nominal operation of the ASPS for solar or stellar pointing first involves coarse gimbal pointing with coarse (wide field of view) sensors onboard the ASPS (or with sensors onboard the carrier vehicle and relative gimbal angle information). The rim centering mode is activated during gimbal slewing. After coarse alignment, coarse roll positioning is accomplished by means of the rim roll motor using information from a relative roll sensor located on the rim or a sensor onboard the ASPS. After coarse attitude alignment, vernier fine pointing is initiated. For this mode, errors obtained from fine (narrow field of view) attitude sensors located on the ASPS system, either as part of the instrument or remote, are nulled by small magnetic-suspension and fine-pointing-actuator torques applied to the annular rim. Also, translation rim centering is accomplished for this mode.

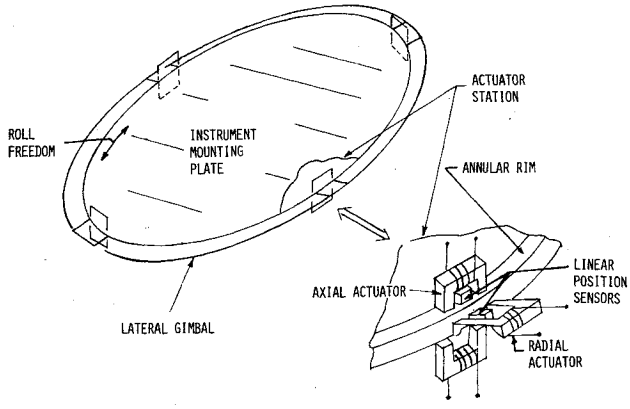

Fig. 6 Vernier pointing assembly configuration.

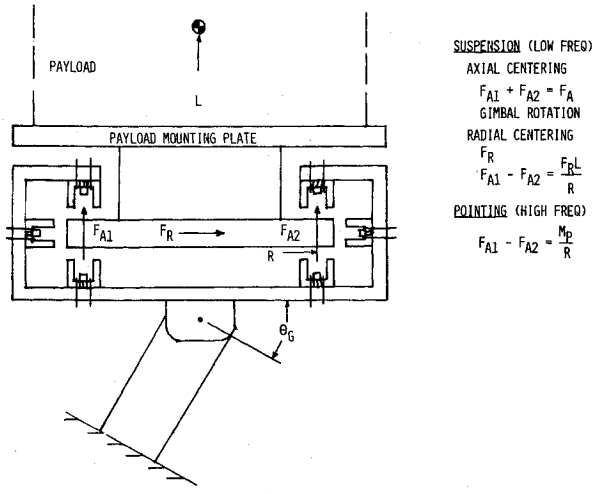

Fig. 7 Simplified ASPS schematic.

Nominal operation of the ASPS for Earth pointing initially involves establishing the correct elevation, lateral, and roll attitudes and attitude rates (slewing) in the rim centering mode. After appropriate smooth instrument slewing is established, vernier pointing (similar to that described for solar and stellar pointing) is accomplished.

Upon completion of a pointing task, connection of appropriate interfaces (data, power, cryogenic) between the vernier pointing assembly and the coarse pointing assembly may take place. These interfaces could be maintained during a pointing task if the pointing degradation caused by the interface connection (wire, tubing, etc.) were tolerable.

Description of Vernier Pointing Assembly

The vernier pointing assembly is shown schematically in Fig. 6 and is similar to the suspension system discussed in Ref. 1. Electromagnets attached to the elevation or the lateral gimbal, working in opposed pairs (both radial and axial) are used to provide fine pointing forces on the rim of the instrument mounting plate. The command forces originate from rim position sensors attached to the lateral gimbal while in the rim centering mode or from instrument pointing error sensors for the axial actuators while in the vernier pointing mode. The radial actuators are always maintained in the rim centering mode. Roll positioning is provided by a linear noncontacting roll torque motor (not shown) which produces forces tangential to the rim. Roll angle is determined from a linear sensor located along or within the periphery of the rim. Thus it is seen that the instrument mounting plate is completely isolated from the elevation gimbal when there are no interface connections, and the only forces produced on it, as long as the electromagnet gaps are maintained, are those

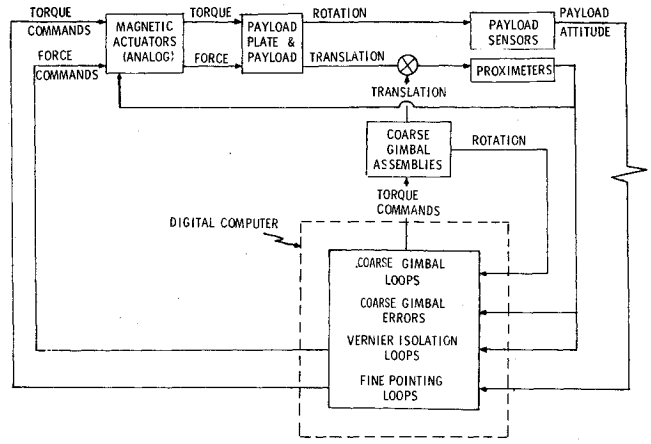

Fig. 8 ASPS block diagram.

produced by the electromagnets themselves, in response to command signals.

Simplified Control System Description

As an aid to understanding the ASPS, Fig. 7 is included. Figure 7 illustrates the fine-pointing concept in two dimensions only. A servoed gimbal with rotational freedom θ_G relative to a carrier is depicted housing three sets of magnetic actuators. These actuators are assumed to produce the three forces F_{A1}, F_{A2}, and F_R on the payload/rim structure and are discussed in more detail at a later point.

The suspension control loops involve axial and radial centering of the payload/rim structure using these actuators at low frequencies. Axial centering is accomplished using forces F_{A1} and F_{A2} to position the rim center at a desired midpoint. The gimbal is then rotated to allow centering the rim edges at midpoints between actuator pole faces. Radial centering is accomplished by the force F_R. However, note that a disturbance moment $F_R L$ is produced on the payload/rim structure, which would result in an intolerable pointing error if left uncompensated. In a forward-loop sense this moment is compensated by producing a simultaneous moment of equal but opposite magnitude with the axial actuators. This compensation allows the use of the ASPS in an end-mount configuration. Fine pointing is achieved using the axial actuators to produce equal and opposite forces of desired magnitudes resulting in a control moment M_P. The fine-pointing control loops are closed around payload sensors using conventional compensation to generate the desired value of M_P.

Figure 8 is a schematic of the fine-pointing control system. There are three types of control loops in operation during fine-pointing (in addition to the roll control loops not shown). The fine-pointing loops use payload sensor pointing data to generate magnetic actuator torques which act on the payload mounting plate. Proximeters, measuring magnetic actuator gaps, are used in the vernier isolation (suspension) loops to generate translation forces which maintain the payload mounting plate centered translationally. These translation forces act through the center-of-mass of the entire payload/sensor/mounting plate mass to avoid fine-pointing loop disturbance inputs. The proximeters are also used to calculate a command signal for the coarse gimbal servo loops which then null the relative angular deviation between the coarse and fine assemblies, and thus keep the rim centered between pole faces.

Description of Magnetic Actuator Concepts

Figure 9 is a sketch of a magnetic actuator. Included are two electromagnetic circuits, with currents I_T and I_B, producing forces F_T and F_B on a segment of the ASPS rim

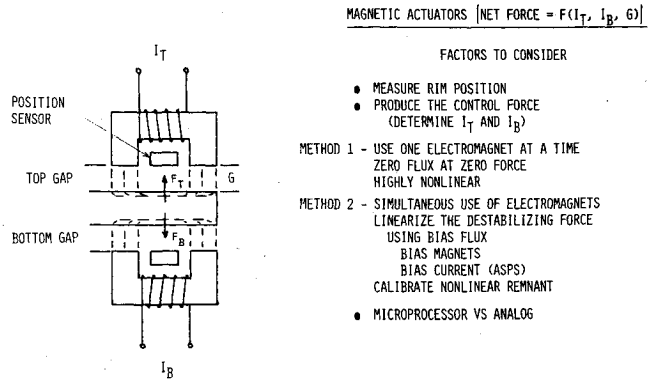

Fig. 9 Schematic representation of a magnetic bearing.

positioned at a gap distance G from the top electromagnet pole face.

Assuming negligible fringing and ignoring nonlinear core effects, the force produced by a given electromagnet is given by

$$F=K(I^2/G^2) \tag{1}$$

A position sensor is shown and is required both for compensating the inverse square effect of gap as well as for use in the isolation loops.

Two methods of magnetic actuator control loop mechanization have been studied theoretically and tested successfully in the lab. The first method uses one electromagnet at a time, the top circuit for an upward force and the bottom for downward (since each circuit can physically only produce a unidirectional force). This method has the advantage of requring no flux for a zero value of net force. However, the method is highly nonlinear and the current must be switched discontinuously when the net force desired goes through zero. One implementation of this method uses analog multiplier and square root modules and produces a direct solution of Eq. (1) for the coil current, i.e.,

$$I=G\sqrt{F_C/K} \tag{2}$$

where F_C is the commanded force.

Another implementation of this method is currently undergoing laboratory tests. In this approach, actual calibration data for a given bearing pair is stored in the memory of a microprocessor system. Using the force command and gap position as input data, the correct value of current input to the coil can be obtained by using a table lookup routine. A straight line approximation is being used to interpolate between points.

The second method of magnetic actuator control loop mechanization involves controlling the upper and lower electromagnets differentially about a flux level. The bias flux can either be supplied by permanent magnets in the magnetic circuit or by bias currents. The force-current characteristic of a flux-biased magnetic actuator with the suspended mass centered in the actuator gaps is shown in Fig. 10. This figure illustrates a linear electromagnet gain of the actuator at a given gap position. It can be shown (Ref. 4) that for small perturbations about a fixed operating point, the effect of motion in the gaps is also linear and the actuator force as a function of differential coil current and displacement can be written as

$$F=K_BI_C+K_MG \tag{3}$$

where K_B is an equivalent electromagnet gain and K_M is an equivalent unbalanced bias flux stiffness. Unfortunately, for different nominal operating points the linear small perturbation electromagnet gain and equivalent unbalanced bias flux stiffness will change. This, in effect, rules out permanent magnet flux bias if an actuator with linear characteristics over a wide gap range is required. One way to linearize the actuator characteristics is to use bias currents and control currents that are a function of gap displacement. This approach adjusts the bias current and control currents of the upper and lower electromagnets so that the bias force produced by each and the net force produced by a given command force is equal no matter where the suspended mass is in the gap. The unbalanced bias flux stiffness is thus eliminated and the electromagnet gain is constant. An implementation of this method is presented in Ref. 6.

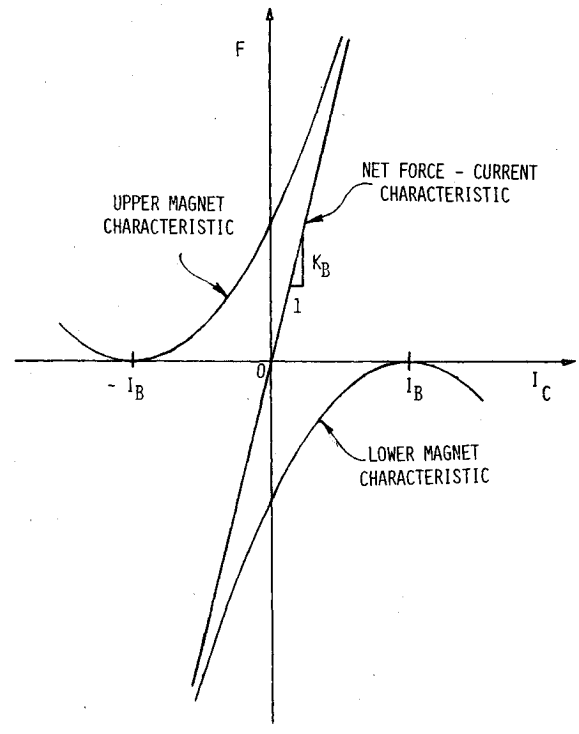

Fig. 10 Force-current characteristic of a flux-biased magnetic actuator.

Simulation Description

A digital computer simulation of the ASPS mounted in the instrument bay of the Space Shuttle has been developed. The simulation includes rigid-body dynamic models of the multibody system and models of the magnetic actuators, payload sensors, coarse gimbal controllers, fine-pointing controller, and a model of a shuttle main reaction control subsystem limit cycling disturbance. A detailed discussion of each of the models comprising the ASPS digital simulation is considered to be beyond the scope of this paper. However, since the approach taken in the development of the vehicle dynamics equations represents a nonstandard technique, it was felt that the inclusion of this development was warranted. A brief description of the rigid-body dynamics model follows.

The spacecraft with ASPS mounted consists of four rigid bodies of constant mass and mass distribution. Three bodies form the composite, constrained model of the shuttle and coarse gimbals shown in Fig. 5. Each body is allowed only rotational freedom with respect to a neighboring body. Attached to the shuttle vehicle is the outer gimbal with one degree-of-freedom relative to the shuttle. Attached to the outer gimbal is the inner gimbal with one degree-of-freedom relative to the outer gimbal. The gimbal axes are assumed to be perpendicular. The payload is the fourth body of the complete system. Mutual forces produced by the magnetic bearings and by a flexible cable linkage provide constraints between the payload and the coarse gimbals.

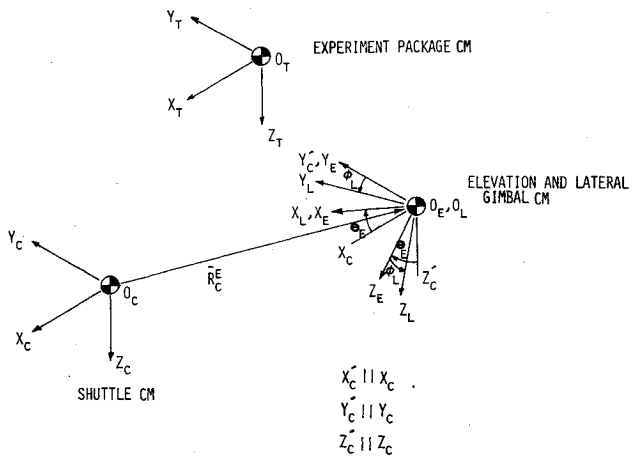

Fig. 11 ASPS dynamics model coordinate systems.

A multibody dynamics model of the shuttle/ASPS system was formulated by a method described in Ref. 7. Using this method, first an expression for the total kinetic energy of the multibody system is constructed. From this expression, the generalized momenta of each of the bodies or composite bodies is found. Expressions for the rate of change of the generalized momenta are then equated to the forces and torques acting between the bodies and upon the system as a whole. This momentum approach yields a 14-DOF nonlinear system which is computationally efficient.

In Fig. 11, the relationship of the centers of mass of the bodies and the relationship of the reference frames is shown. Referring to this figure, the kinetic energy of the carrier vehicle is written as

$$\mathrm{KE}_C = \tfrac{1}{2} M_C \bar{V}_C' \bar{V}_C + \tfrac{1}{2} \bar{\omega}_C' I_C \bar{\omega}_C \tag{4}$$

Also, the velocity of the point 0_E in the E frame is

$$\bar{V}_E = D_{EC}(\bar{V}_C + \bar{\omega}_C \times \bar{R}_C^E) \tag{5}$$

and the body rates are

$$\bar{\omega}_E = \bar{\dot{\theta}}_E + D_{EC}\bar{\omega}_C \tag{6}$$

where

$$D_{EC} = \begin{bmatrix} \cos\theta_E & 0 & -\sin\theta_E \\ 0 & 1 & 0 \\ \sin\theta_E & 0 & \cos\theta_E \end{bmatrix} \tag{7}$$

The kinetic energy of the elevation gimbal is

$$\mathrm{KE}_E = \tfrac{1}{2} M_E \bar{V}_E' \bar{V}_E + \tfrac{1}{2} \bar{\omega}_E' I_E \bar{\omega}_E \tag{8}$$

which can be expanded to

$$\mathrm{KE}_E = \tfrac{1}{2} M_E \bar{V}_C' \bar{V}_C + M_E \bar{V}_C' (\bar{\omega}_C \times \bar{R}_C^E) + \tfrac{1}{2} \bar{\omega}_C' I_C^E \bar{\omega}_C + \tfrac{1}{2} \bar{\omega}_E' I_E \bar{\omega}_E \tag{9}$$

where

$$\bar{\omega}_C' I_C^E \bar{\omega}_C = M_E (\bar{\omega}_C \times \bar{R}_C^E)' (\bar{\omega}_C \times \bar{R}_C^E) \tag{10}$$

Then the velocity of the point 0_L in the L frame is

$$\bar{V}_L = D_{LE} \bar{V}_E \tag{11}$$

and the body rates are

$$\bar{\omega}_L = \bar{\dot{\phi}}_L + D_{LE}\bar{\omega}_E \tag{12}$$

where

$$D_{LE} = \begin{bmatrix} 1 & 0 & 0 \\ 0 & \cos\phi_L & \sin\phi_L \\ 0 & -\sin\phi_L & \cos\phi_L \end{bmatrix} \tag{13}$$

These become

$$\bar{V}_L = D_{LE} D_{EC} (\bar{V}_C^C + \bar{\omega}_C \times \bar{R}_C^E) \tag{14}$$

and

$$\bar{\omega}_L = \begin{Bmatrix} \dot{\phi}_L \\ 0 \\ 0 \end{Bmatrix} + D_{LE} \left(\begin{Bmatrix} 0 \\ \dot{\theta}_E \\ 0 \end{Bmatrix} + D_{EC}\bar{\omega}_C \right) \tag{15}$$

Then the kinetic energy of the lateral gimbal is given by

$$\mathrm{KE}_L = \tfrac{1}{2} M_L \bar{V}_L' \bar{V}_L + \tfrac{1}{2} \bar{\omega}_L' I_L \bar{\omega}_L \tag{16}$$

which is expanded into

$$\mathrm{KE}_L = \tfrac{1}{2} M_L \bar{V}_C' \bar{V}_C + M_L \bar{V}_C' (\bar{\omega}_C \times \bar{R}_C^E) + \tfrac{1}{2} \bar{\omega}_C' I_C^L \bar{\omega}_C + \tfrac{1}{2} \bar{\omega}_L' I_L \bar{\omega}_L \tag{17}$$

where

$$\bar{\omega}_C' I_C^L \bar{\omega}_C = M_L (\bar{\omega}_C \times \bar{R}_C^E)' (\bar{\omega}_C \times \bar{R}_C^E) \tag{18}$$

The total kinetic energy of the 8-DOF carrier system is formed by summing the kinetic energy of the component parts. Collecting and simplifying, the total kinetic energy of the system is given by

$$\mathrm{KE}_{CEL} = \tfrac{1}{2} M_{CEL} \bar{V}_C' \bar{V}_C + M_{EL} \bar{V}_C' (\bar{\omega}_C \times \bar{R}_C^E) + \tfrac{1}{2} \bar{\omega}_C' I_C^{CEL} \bar{\omega}_C + \tfrac{1}{2} \bar{\omega}_E' I_E \bar{\omega}_E + \tfrac{1}{2} \bar{\omega}_L' I_L \bar{\omega}_L \tag{19}$$

where

$$M_{EL} = M_E + M_L \tag{20}$$

$$M_{CEL} = M_C + M_E + M_L \tag{21}$$

$$I_C^{CEL} = I_C + I_C^E + I_C^L \tag{22}$$

The Lagrangian equations for quasi-coordinates are developed as described on pp. 157-160 in Ref. 8. Partial derivatives of the total kinetic energy with respect to the quasi-degrees-of-freedom yield the generalized momentum associated with that degree of freedom:

$$\bar{H}_L = \frac{\partial \mathrm{KE}_{CEL}}{\partial \bar{\omega}_L} = I_L \bar{\omega}_L \tag{23}$$

$$\bar{H}_E = \frac{\partial \mathrm{KE}_{CEL}}{\partial \bar{\omega}_E} = I_E \bar{\omega}_E + D_{LE}' I_L \bar{\omega}_L \tag{24}$$

$$\bar{H}_C = \frac{\partial \mathrm{KE}_{CEL}}{\partial \bar{\omega}_C} = M_{EL} (\bar{R}_C^E \times \bar{V}_C) + I_{CEL}\bar{\omega}_C + D_{EC}' (I_E \bar{\omega}_E + D_{LE}' I_L \bar{\omega}_L) \tag{25}$$

$$\bar{P}_C = \frac{\partial \mathrm{KE}_{CEL}}{\partial \bar{V}_C} = M_{CEL}\bar{V}_C + M_{EL}(\bar{\omega}_C \times \bar{R}_C^E) \tag{26}$$

To simplify the development, the dynamic equations are written in matrix form. Constraint torques are eliminated in the differential equations by eliminating those equations that contain constraint torques (Ref. 7, p. 4). The components of angular velocity and momentum along the eliminated axes are derived through the constraint relationship.

$$\frac{d\bar{H}_L}{dt} + \bar{\omega}_L \times \bar{H}_L = \bar{T}_L - \bar{T}_{MBA} \tag{27}$$

$$\frac{d\bar{H}_E}{dt} + \bar{\omega}_E \times \bar{H}_E = \bar{T}_E - \bar{D}'_{LE}\bar{T}_{MBA} \tag{28}$$

$$\frac{d\bar{H}_C}{dt} + \bar{\omega}_C \times \bar{H}_C = \bar{T}_C - D'_{EC}D'_{LE}\bar{T}_{MBA} - \bar{R}_C^E \times D'_{EC}D'_{LE}\bar{F}_{MBA} \tag{29}$$

$$\frac{d\bar{P}_C}{dt} + \bar{\omega}_C \times \bar{P}_C = \bar{F}_C - D'_{EC}D'_{LE}\bar{F}_{MBA} \tag{30}$$

The kinetic energy of the payload is

$$\mathrm{KE}_{PL} = \tfrac{1}{2}M_{PL}\bar{V}'_{PL}\bar{V}_{PL} + \tfrac{1}{2}\bar{\omega}'_{PL}I_{PL}\bar{\omega}_{PL} \tag{31}$$

Partial derivatives of the kinetic energy with respect to the quasi-degrees-of-freedom are given by

$$\bar{H}_{PL} = \frac{\partial \mathrm{KE}_{PL}}{\partial \bar{\omega}_{PL}} = I_{PL}\bar{\omega}_{PL} \tag{32}$$

$$\bar{P}_{PL} = \frac{\partial \mathrm{KE}_{PL}}{\partial \bar{V}_{PL}} = M_{PL}\bar{V}_{PL} \tag{33}$$

The dynamic equations are then

$$\frac{d\bar{H}_{PL}}{dt} + \bar{\omega}_{PL} \times \bar{H}_{PL} = \bar{T}_{MBA} + \bar{R}_{PL}^B \times \bar{F}_{MBA} \tag{34}$$

$$\frac{d\bar{P}_{PL}}{dt} + \bar{\omega}_{PL} \times \bar{P}_{PL} = \bar{F}_{MBA} \tag{35}$$

where $\bar{T}_{MBA}$ and $\bar{F}_{MBA}$ are the torques and forces produced by the magnetic bearing assembly and $\bar{T}_L$ and $\bar{T}_E$ are the interbody torques produced by the coarse gimbal actuators. $\bar{T}_C$ and $\bar{F}_C$ are the external disturbance torques applied to the shuttle vehicle.

In the digital simulation, numerical solution proceeds by first defining an initial vehicle state. From this state information, all forces and torques are computed from magnetic bearing models, coarse gimbal models and external disturbances. Then the momentum derivatives are integrated to yield a new momentum state. These moments are used to solve for a new set of body rates and velocities which are then input to kinetic relations. After a new vehicle state has been defined, the process is repeated.

The ASPS functions in three modes of operation: 1) fine-pointing of the payload, 2) centering the payload in the magnetic actuator assembly, and 3) tracking the payload mounting plate and shuttle motions by the coarse gimbals. Simulations performed for the ASPS in the fine-pointing mode including magnetic actuator nonlinearities, proximeter noise, perfect sensors, sensor estimators, and a shuttle main reaction control system firing about the pitch axis yielded a peak pointing error of 0.0034 arcsec. The error increased to 0.056 arcsec when a flexible cable was used for power and data transfer from the coarse assembly to the vernier assembly. When noise was added to the rate gyro and star tracker, the peak pointing error was less than 0.1 arcsec. In order to determine a worst-case error under the assumptions of the simulation, no attempt was made to compensate for the cable inputs with compensating control inputs.

Concluding Remarks

This paper has presented a description of the ASPS configured as an end-mount pointing system. The paper has also presented some of the background research and evaluation that led to the ASPS concept and to the selection of the end-mount configuration for prototype development and flight test. The system offers the potential for isolating and fine-pointing shuttle experiments to very low values of stability error and has been configured to meet the needs of the experiment community by allowing minimum size and shape constraints on the experiments themselves.

References

[1] Anderson, W. W. and Groom, N. J., "The Annular Momentum Control Device (AMCD) and Potential Applications," NASA TN D-7866, 1975.

[2] Anderson, W. W. and Joshi, S. M., "The Annular Suspension and Pointing (ASP) System for Space Experiments and Predicted Pointing Accuracies," NASA TR R-448, 1975.

[3] Anderson, W. W. and Groom, N. J., "Magnetic Suspension and Pointing System," U.S. Patent 4,088,018, May 9, 1978.

[4] Ball Brothers Research Corp., "Annular Momentum Control Device (AMCD)," Vols. I and II, NASA CR-144917, 1976.

[5] Groom, N. J. and Terray, D. E., "Evaluation of a Laboratory Test Model Annular Momentum Control Device," NASA TP-1142, 1978.

[6] Cunningham, D. C., Gismondi, T. P., and Wilson, G. W., "System Design of the Annular Suspension and Pointing System (ASPS)," AIAA Paper 78-1311, AIAA Guidance and Control Conference, Palo Alto, Calif., Aug. 1978.

[7] Russell, W. J., "Dynamic Analysis of the Communication Satellites of the Future," AIAA Paper 76-261, AIAA/CASI 6th Communications Satellite Systems Conference, Montreal, Canada, April 5-8, 1976.

[8] Meirovitch, L., *Methods of Analytical Dynamics*, McGraw-Hill, Inc., New York, 1970, pp. 157-160.